RESEARCH ARTICLE

Graphene surface plasmon sensor for ultra-low-level SARS-CoV-2 detection

Md. Mahbub Hossain [ID], **Muhammad Anisuzzaman Talukder** [ID]*

Department of Electrical and Electronic Engineering, Bangladesh University of Engineering and Technology, Dhaka, Bangladesh

* anis@eee.buet.ac.bd

Abstract

Precisely detecting the ultra-low-level severe acute respiratory syndrome coronavirus 2 (SARS-CoV-2) is crucial. The detection mechanism must be sensitive, low-cost, portable, fast, and easy to operate to tackle coronavirus disease 19 (COVID-19). This work proposes a sensor exploiting graphene surface plasmon resonance to detect SARS-CoV-2. The graphene layer functionalized with angiotensin-converting enzyme 2 (ACE2) antibodies will help efficient adsorption of the SARS-CoV-2. In addition to the graphene layer, ultra-thin layers of novel two-dimensional materials tungsten disulfide (WS_2), potassium niobate ($KNbO_3$), and black phosphorus (BP) or blue phosphorus (BlueP) used in the proposed sensor will increase the light absorption to detect an ultra-low SARS-CoV-2 concentration. The analysis presented in this work shows that the proposed sensor will detect SARS-CoV-2 as small as ~ 1 fM. The proposed sensor also offers a minimum sensitivity of 201 degrees/RIU, a figure-of-merit of 140 RIU^{-1}, and enhanced binding kinetics of the SARS-CoV-2 to the sensor surface.

1 Introduction

Severe acute respiratory syndrome coronavirus 2 (SARS-CoV-2) is a critical biological pathogen responsible for coronavirus disease 2019 (COVID-19). Recently, COVID-19 has caused an unprecedented health problem worldwide due to the high progression rate of fatality. SARS-CoV-2 is a positive-sense single-stranded ribonucleic acid (RNA) virus [1]. Several research groups have proposed and demonstrated efficient, cost-effective, and real-time detection techniques for the SARS-CoV-2 virus [2–8]. Culture-based techniques that detect nucleic acid or proteins and serological-based techniques that detect the created antibodies are commonly used for virus diagnosis [9]. Recent advances in molecular technology have led to the development of nucleic acid-dependent amplification techniques for virus detection, e.g., the reverse transcriptase quantitative polymerase chain reaction (RT-qPCR) technique. RT-qPCR is known as the gold standard for detecting several critical viruses, such as SARS-CoV-2, human immunodeficiency virus (HIV), and cytomegalovirus (CMV) [2].

RT-qPCR is highly sensitive and selective for SARS-CoV-2 detection [3]. Nevertheless, its application is limited due to significant false-negative cases ($\sim 15\%$), long processing time,

costly instruments, and the requirement of skilled human resources and uninterrupted power supply over a long period [4, 5]. Conversely, colorimetric-based loop-mediated isothermal amplification (LAMP) techniques have been proposed for SARS-CoV-2 detection to overcome the limitations of an RT-qPCR technique [5]. LAMP techniques show a high nucleic-acid amplification efficiency but are time-consuming and tedious as they use electrophoresis for detection. Additionally, the decision regarding the color change of reaction vessels by human eyes is potentially a subjective issue and may significantly impact the test results [6]. A chest computer tomography (CT) scan can also be used to detect the SARS-CoV-2 [7]. However, such a technique cannot be used for asymptomatic patients, early-stage detection, and the measurement of the mass density of virus [10]. Serological tests, e.g., enzyme-linked immuno-sorbent assay (ELISA), can also be used for SARS-CoV-2 diagnosis [8]. Serological methods have shown high efficiency and are low-cost, but they suffer from low sensitivity (S) and false-negative reports [3].

In the last few years, optical sensors based on plasmonics have attracted significant attention in virus detection due to their simplicity, flexibility, label-free operation, and short response time [2, 11–15]. Plasmonics-based optical sensors have been proposed to detect many critical pathogens, such as dengue virus envelope (E)-protein, thyroglobulin, HIV-1, and SARS-CoV-2 [3, 16–20]. Besides, optical biosensors have recently been proposed to detect SARS-CoV-2 proteins, such as spike and nucleo-capsid [21–25]. In particular, a toroidal plasmonic meta-sensor has recently been proposed to detect SARS-CoV-2 spike (S)-protein using terahertz (THz) wavelength signal, demonstrating a limit of detection (LoD) of only ~ 4.2 fM [19]. However, the plasmonic meta-sensor suffers from insensitivity to S-protein concentration between 20 and 50 fM and low quality-factor (Q-factor).

More recently, a surface plasmon resonance (SPR) based method has been proposed to examine the affinity of SARS-CoV-2 S-protein to angiotensin-converting enzyme 2 (ACE2) [26]. Additionally, plasmonic photo-thermal effect and localized SPR (LSPR) have been proposed to detect selected sequences of SARS-CoV-2 by nucleic acid hybridization techniques [4]. However, thermo-plasmonic heat cannot discriminate between two similar gene sequences, and a sensor employing this effect shows low detection accuracy. Furthermore, a near-infrared (NIR) plasmonic sensor has been suggested for SARS-CoV-2 S-protein detection using a phase interrogation technique [3]. Although an NIR plasmonic sensor shows high sensitivity, its performance is limited due to the complex technology required for phase variation measurement.

Recently, graphene surface plasmon (SP) has drawn significant interest for application in sensing due to two-dimensional (2-D) graphene's promising properties, such as high π-conjugation structure, shallow thickness and mass, and high mechanical strength [27]. In SPR sensors, the sample bio-molecules should be efficiently adsorbed by the sensor surface to increase the sensitivity [28–30]. Therefore, bio-molecular recognition elements (BREs) are often placed on top of SPR-based sensors to functionalize the metal film for enhanced bio-molecule adsorption. Since graphene surfaces can be modified by introducing different BRE functional groups, such as epoxy, hydroxyl, ketone, and carboxyl in their basal plane, graphene-based sensors show high bio-molecule adsorption capability [31]. Recently, apart from graphene, a few other 2-D materials, such as molybdenum disulfide (MoS_2) and blue phosphorus (BlueP), have been shown to significantly improve sensor sensitivity when used in simple metal-based SPR sensors [32]. Moreover, an SPR biosensor based on bimetallic films gold (Au)-silver (Ag) and BlueP has shown good sensitivity [33] but limited performance in detecting ultra-low concentrations of biological molecules. However, using different 2-D materials like tungsten disulfide (WS_2), potassium niobate ($KNbO_3$), and black phosphorus (BP) in addition to graphene in a

silver (Ag) based SPR biosensor is still unexplored, although they have optical properties promising for an SPR sensor.

This work proposes a graphene SPR sensor for ultra-low-level SARS-CoV-2 detection. SPR plays a pivotal role in the sensing principle of the proposed sensor [34–36]. The proposed sensor is based on the Kretschmann configuration, thus being simple. ACE2 functionalizes the graphene layer for efficient adsorption of the SARS-CoV-2 S-protein sample [20]. The proposed sensor uses thin layers of novel 2-D materials between graphene and Ag layers, such as WS_2, $KNbO_3$, and BP or BlueP, to increase the light absorption and hence, the sensor's sensitivity. The optical and electronic properties of 2-D hetero-structures highly depend on the number of 2-D material layers and the stacking patterns. Due to their excellent sensitivity enhancement effects, such as 2-D materials BlueP/BP, $KNbO_3$, and WS_2, we believe our proposed biosensor will find applications in practical biosensing [37].

This work is a theoretical work based on detailed analytical and numerical calculations. We apply the finite difference time domain (FDTD) simulation technique to characterize the sensor response to incident light and determine the sensor performance parameters. SARS-CoV-2 S-proteins are detected by calculating the change in resonance angle for SPR excitation. We use the Langmuir model to calculate the equilibrium dissociation constant (K_D) to determine the binding kinetics between ACE2 and S-protein [16]. The proposed sensor shows the prospect of detecting ultra-low SARS-CoV-2 concentration of only ~ 1 fM, which is crucial for the early detection of this deadly virus. The proposed graphene SPR sensor also shows a high sensitivity, figure-of-merit (FoM), selectivity, and resolution while detecting the SARS-CoV-2 compared to the state-of-the-art SPR sensors. Furthermore, the proposed sensor offers a significantly small K_D, showing enhanced binding of SARS-CoV-2 on the sensor surface.

The rest of the paper is prepared as follows: Sec. 2 illustrates and discusses the proposed sensor configuration and optimization of layer thicknesses. Then, Sec. 3 presents the optical properties of different materials, theoretical analysis of sensor performance parameters, and simulation methods. Next, we present and discuss the SARS-CoV-2 detection approach, analysis of binding between ACE2 and S-protein, and the calculated sensor performances in Sec. 4. Finally, in Sec. 5, we conclude the proposed sensor results.

2 Proposed sensor

2.1 Configuration

The proposed graphene SPR sensor is designed based on the Kretschmann configuration, as shown in Fig 1. The incident light on the metal–dielectric interface at the resonance angle (θ_r) excites SPR, significantly absorbing the incident light. The θ_r for SPR changes based on the refractive index of the dielectric material, i.e., the sample layer. The sample layer refractive index varies due to the presence of SARS-CoV-2. Therefore, SARS-CoV-2 can be detected by measuring the change in θ_r. SARS-CoV-2 samples will be placed on the top surface of the proposed sensor structure, which is a graphene layer. In practice, we need binding molecules to immobilize antibodies on the graphene surface to capture SARS-CoV-2. We use 1-pyrenebutyric acid N-hydroxy-succinimide ester (PBASE) that permits the binding of functional groups to graphene without disrupting the carbon atomic structure [38] and acts as an interfacing molecule and a probe linker [20]. PBASE contains an aromatic pyrenyl group, which physically interacts with graphene through π–π interaction. PBASE also contains a succinimidyl ester group, which covalently reacts with the amino group on the antibody by an amide bond [39].

SARS-CoV-2 consists of four fundamental physical proteins: S, E, matrix, and nuclei-capsid proteins. S-protein is immunogenic and shows amino acid sequence variation, permitting the
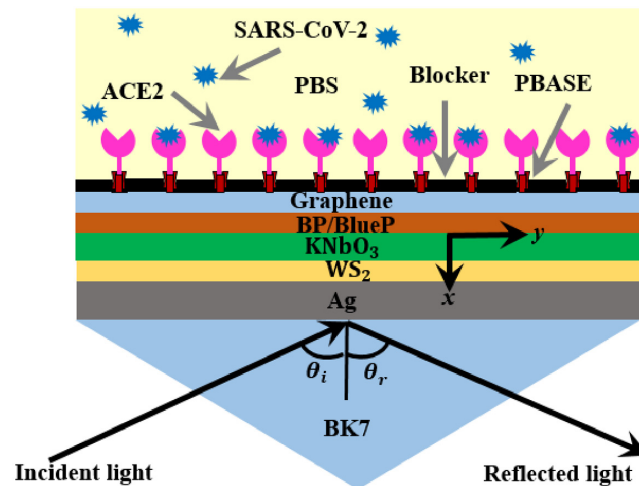
Fig 1. Schematic illustration of the proposed graphene SPR sensor for SARS-CoV-2 S-protein detection.

specific detection of SARS-CoV-2 [40]. Hence, this work uses S-protein as the sensing element to identify SARS-CoV-2 [20]. The S-protein contains protrusions that only bind to specific receptors on the host cell, such as ACE2, dipeptidyl peptides-4, amino-peptides N, and carcinoembryonic antigen-related cell adhesion molecule 1 [41]. Recent research results have confirmed that ACE2 is an effective receptor for SARS-CoV-2 S-protein, with SARS-CoV-2 grasping ACE2 cells primarily by endocytosis [42]. Therefore, thiol-tethered DNA is used in this work as an ACE2 layer for receiving and detecting SARS-CoV-2 samples [43].

In this work, ACE2 antibodies are placed throughout the top surface of the sensor with 50 nm separations between the neighboring ACE2 antibodies. ACE2 height and width are assumed to be 3 nm and 2.1 nm, respectively [17]. To block the free space between ACE2 antibodies, we use ethanolamine as a blocker [44]. Each ethanolamine blocker is 3.5 nm long and separated from neighboring blockers by 50 nm. The ethanolamine blockers support keeping the ACE2 antibodies static in their places and prevent the adsorption of non-specific elements on the graphene surface [45]. SARS-CoV-2 samples can be collected from human nasopharyngeal swabs and preserved in a phosphate-buffered saline (PBS) solution [46]. The PBS solution containing SARS-CoV-2 S-proteins makes the sensing layer, which can flow over the sensor surface through a flow channel as an analyte [45]. In this work, the PBS sensing layer volume is set to 100 μL and 200 μL to investigate the sensor performances. We note that the PBS is neutral to the SARS-CoV-2 S-protein and often used for analyzing proteins [47].

The proposed graphene SPR sensor is built on a semi-infinite boro-silicate (BK7) prism material, as shown in Fig 1. The light is incident on the multi-layer structure from the prism side, and the reflected light is recorded on the same side. The incident light excites surface plasmon polaritons (SPPs) at the metal–dielectric, i.e., metal–multi-layer interface. The excitation of plasmonic modes is sensitive to the thickness of the metal layer. This work uses a 46-nm-thick Ag layer as this thickness peaks the SPP excitation [48]. For SPR, Ag is preferred to other metals, such as Au or copper (Cu), as it shows dense plasmonic interaction with light at low loss [49]. The scattering cross-section of Ag is greater than other metal choices [50]. Besides, Ag offers a narrower SPR spectrum than other metals, which is essential for plasmonic biosensors.

The multi-layer 2-D structure interfaces with the metal layer with WS_2. To date, MoS_2 has been commonly used for such planar plasmonic structures. MoS_2 and WS_2 belong to the same family of chemical characteristics. However, WS_2 is more stable than MoS_2, especially at high temperatures [51]. Additionally, WS_2 effectively absorbs more light than MoS_2 or other transition metal dichalcogenide (TMD) materials [52, 53]. Therefore, WS_2 helps decrease the incident light's reflection when interfaced with Ag.

In the proposed structure, a $KNbO_3$ layer follows the WS_2 layer. $KNbO_3$ has a high optical permittivity that enhances the electric flux density within the sensor [54]. Additionally, the imaginary part of the refractive index of $KNbO_3$ is zero. Hence, $KNbO_3$ increases the light confinement without incurring losses. The layer that follows $KNbO_3$ is a phosphorene family material BP or BlueP. The BP or BlueP layer is sandwiched between $KNbO_3$ and graphene. The sensitivity of the proposed sensor increases significantly as BP and BlueP have a high real part of the refractive index, enhancing the light confinement [55].

Using several 2-D materials in the proposed structure will increase the fabrication complexity slightly. However, the fabrication of various 2-D materials is usually cheap nowadays. In addition, the significant performance enhancement from the proposed sensor justifies using different 2-D materials at a reasonable cost increase. Furthermore, the sensor will be available for reuse after the purification of the used sensing channel.

2.2 Optimization of layer thicknesses

The proposed graphene SPR sensor has several layers, each having an essential effect on the overall performance. However, appropriate optimization of layer thicknesses is critical to get the best response from the proposed sensor. Here, we have optimized the layer thicknesses of the proposed sensor using the approach discussed in Refs. [56, 57]. In particular, we examine the effect of each layer thickness on the reflected light intensity (R) profile as a function of the incidence angle (θ_i). The optimization of layer thicknesses depends on the minimum reflected light intensity (R_{min}) and full-width at half-maximum (FWHM) of the R-profile. The FWHM is the spectral width of the R-profile corresponding to 50% reflectivity (FWHM = $\Delta\theta_{i,(0.5)}$) [58]. While the light absorption is maximum on the sensor surface at R_{min}, the FWHM represents the loss in the metal layer. Therefore, both R_{min} and FWHM are crucial for the sensitivity enhancement of a sensor, and an optimized layer thickness should produce both R_{min} and FWHM as small as possible.

The layer thicknesses are optimized sequentially. First, the layer thickness of WS_2 is optimized, and then that of $KNBO_3$, BP, and graphene. To optimize the layer thicknesses, we change each layer thickness while the thicknesses of all other layers are fixed. We optimize the WS_2 layer thickness from calculations, as shown in Fig 2(a). When $WS_2 = 0.8$ nm, R_{min} and FWHM show minimum values. Furthermore, the increase of the WS_2 thickness (d_{WS_2}) broadens the FWHM of R-profiles as R_{min} value increases. Therefore, we set $d_{WS_2} = 0.8$ nm for the proposed sensor structure. Subsequently, we calculate the effects of $KNbO_3$ keeping d_{WS_2} at the optimized value. We determine R_{min} and FWHM values when the thickness of $KNbO_3$ (d_{KNbO_3}) is varied from 10 nm to 14 nm, as shown in Fig 2(b). In this case, both R_{min} and FWHM are minimum when $d_{KNbO_3} = 12.2$ nm.

Following a similar procedure, we optimize d_{BP} and d_{BlueP} when d_{Ag}, d_{WS_2}, and d_{KNbO_3} are at their optimized values. We show the change in R and FWHM with d_{BP} and d_{BlueP} in Fig 2(c). We note that, initially, R decreases very minutely with d_{BP} and is minimum at $d_{BP} = 1.59$ nm. However, R increases when $d_{BP} > 1.59$ nm. By contrast, FWHM always increases with d_{BP} and is minimum when $d_{BP} = 0.53$ nm, which is BP mono-layer thickness. We find that when d_{BP} increases from 0.53 nm to 1.59 nm, R_{min} decreases by 0.52% whereas FWHM increases by
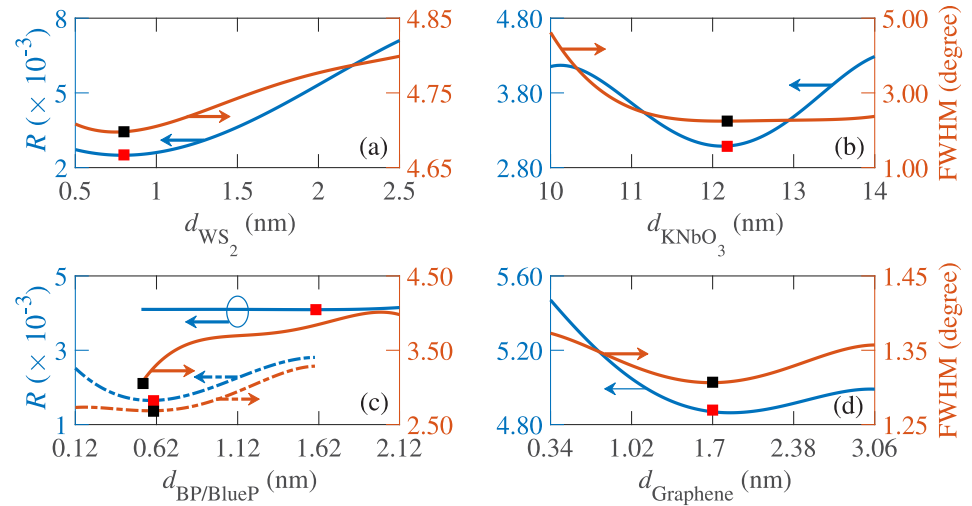
Fig 2. Reflectance (R) of the proposed sensor structure in Kretschmann configuration against layer thicknesses of (a) WS$_2$, (b) KNbO$_3$, (c) BP (solid) and BlueP (dashed), and (d) Graphene.

16.66%. A narrow FWHM of the R-profile is required for high signal-to-noise ratio (SNR) and accuracy of θ_r detection [59]. Therefore, $d_{BP} = 0.53$ nm is set for the proposed structure. We note that R decreases initially with d_{BlueP} and is minimum at $d_{BlueP} = 0.615$ nm. However, R increases when $d_{BlueP} > 0.615$ nm. The thickness of a BlueP single layer is 0.123 nm [60]. Therefore, 0.615 nm represents five layers of BlueP. On the other hand, FWHM decreases slightly and becomes minimum at $d_{BlueP} = 0.615$ nm. Therefore, we set $d_{BlueP} = 0.615$ nm for the proposed structure.

The change of graphene layer thickness changes the surface plasmon wave vector, eventually changing θ_r. Fig 2(d) shows that, as $d_{Graphene}$ increases, both R and FWHM decrease since the incident light confinement at the metal–dielectric interface enhances [58]. When $d_{Graphene}$ increases from mono-layer, i.e., 0.34 nm, to five layers, i.e., 1.70 nm, R decreases by 12.93% as the absorption of incident light increases. However, R_{min} and FWHM both increase when $d_{Graphene} > 1.70$ nm [58]. Therefore, the proposed sensor uses $d_{Graphene} = 1.70$ nm.

3 Modeling and simulation

3.1 Optical properties

The optical properties of the proposed sensor's layer materials are dispersive. Therefore, the sensor's response depends on the incident light's wavelength. The sensor has been designed for an incident wavelength of 633 nm, frequently used in experiments [67]. This work calculates the wavelength-dependent refractive index of the BK7 prism following the discussion presented in Ref. [58] and of Ag using the Drude-Lorentz model [61].

The wavelength-dependent refractive index of WS$_2$ has been calculated using [62]

$$n_{WS_2} = \sqrt{\frac{1}{2}\left[N + \frac{\delta}{\alpha}\right] \pm \frac{1}{2}\sqrt{\left[N + \frac{\delta}{\alpha}\right]^2 - 4n_0^2 n_{sub}^2}}, \tag{1}$$

where $N = n_0^2 + n_{sub}^2$, n_0 and n_{sub} are the refractive indices of air and substrate, respectively.

The parameter δ is the fractional change of the complex reflection ratio, and α is defined as

$$\alpha = 4ik_0 \ d_{\mathrm{WS}_2} \ \frac{n_0 n_{\mathrm{sub}}^2 \cos\theta_i \sin^2\theta_i}{(n_0^2 - n_{\mathrm{sub}}^2)[n_{\mathrm{sub}}^2 - n_0^2 + N\cos(2\theta_i)]}, \tag{2}$$

where $k_0 = 2\pi/\lambda$ and λ is the operating wavelength. The refractive index of KNbO$_3$ depends on λ according to the following expression [63]

$$n_{\mathrm{KNbO}_3} = \sqrt{4.4222 + \frac{0.09972}{\lambda^2 - 0.05496} - 0.01976\lambda^2}. \tag{3}$$

We have used the refractive index of BP from Ref. [64]. Furthermore, the refractive index of graphene has been calculated by [66]

$$n_{\mathrm{Graphene}} = 3 + i\frac{C_G}{3}\lambda, \tag{4}$$

where C_G is a constant with a value of 5.44 μm^{-1} [68]. The calculated refractive indices for BK7, Ag, WS$_2$, KNbO$_3$, BP, and graphene are given in Table 1. The indices of PBASE, ACE2, blocker, and PBS solution of the proposed sensor are obtained from the literature and are also given in Table 1.

The index of the sensing layer (n_s) varies according to the following expression when SARS-CoV-2 S-proteins bind to ACE2 antibodies in the PBS layer [69]

$$n_s = n + \beta D, \tag{5}$$

where n is the index of the PBS solution, β is the index progress coefficient with a value of ~ 0.186 cm^3/gm for PBS [70, 71], and D is the mass density of S-protein in gram per deciliter. We calculate D using the following expression [48]

$$D = C \times M, \tag{6}$$

where C is the S-protein molar concentration in the PBS solution, and M is the S-protein molecular weight, which is 180 kDa or 180×2.5875×10^{-19} gm [42, 72]. We can write 1

Table 1. Refractive indices and thicknesses of the proposed sensor layers.

Material	Refractive index	Thickness (nm)	Reference
ACE2	1.13	2.10	[43]
Blocker	1.4539	3.23	[44]
PBASE	1.74	1.13	[45]
Sensing layer	1.3348	100	[47]
BK7	1.515	semi-infinite	[58]
Ag	Real: 0.055	46	[61]
	Imag: 4.285		
WS$_2$	Real: 4.90	0.8	[62]
	Imag: 0.3124		
KNbO$_3$	2.165	12.20	[63]
BP	Real: 3.50	0.53	[64]
	Imag: 0.01		
BlueP	Real: 2.1666	0.615	[65]
	Imag: 0.1005		
Graphene	Real: 3.0	1.70	[66]
	Imag: 1.1419		
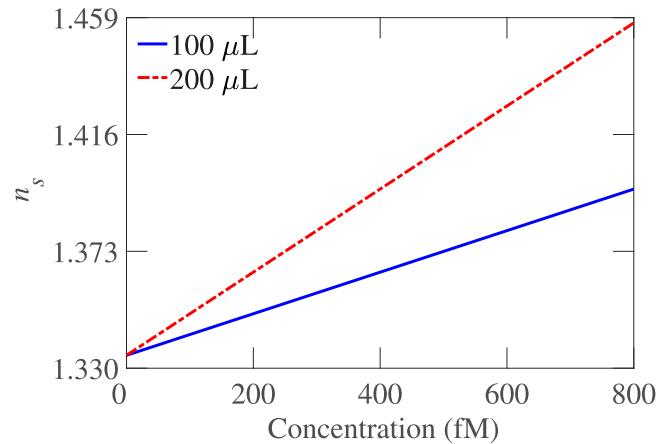
Fig 3. Sensing layer refractive index (n_s) vs. SARS-CoV-2 S-protein concentration for 100-μL and 200-μL PBS solutions.

fM = 1×10^{-15} gm $\times$ 411.04 gm/L, or = 4.1104×10^{-12} gm/dL. Also, 1 fM dissolved in 100 μL PBS solution is equivalent to $4.1104 \times 10^{-12} \times 100 \times 10^{-6}$ gm/dL. Therefore,
$D = 4.1104 \times 10^{-12} \times 100 \times 10^{-6}/10^{-15}$ gm/ dL $\simeq$ 0.041104 gm/dL for 100 μL PBS solution.
Then $n_s = 0.041104 \times 0.00186 + 1.3348 \simeq 1.33485$ for 1 fM S-protein concentration in 100 μL PBS saline.

A similar procedure is applied for the 200-μL PBS solution to determine n_s for varying S-protein concentrations.

In this work, we consider 100-μL and 200-μL PBS in the sensing layer separately, where the molar mass of PBS is 411.04 gm/L. We vary the SARS-CoV-2 S-protein concentration from zero to 800 fM in the PBS solution. The sensing layer refractive index n_s, due to the inclusion of the SARS-CoV-2 S-protein, is calculated using Eqs (5) and (6) and presented in Fig 3. When the S-protein concentration is zero, the refractive index of the sensing layer is 1.3348, which increases linearly as the S-protein concentration increases. We note that 200-μL PBS shows a higher n_s than 100-μL PBS as the mass density of S-protein increases with the PBS solution volume.

3.2 Sensor performance parameters

The sensitivity (S) and FoM are the main performance parameters of SPR-based sensors. These parameters are determined using the R-profile. The sensitivity is defined as the ratio of $\Delta\theta_r$ and Δn_s [73]
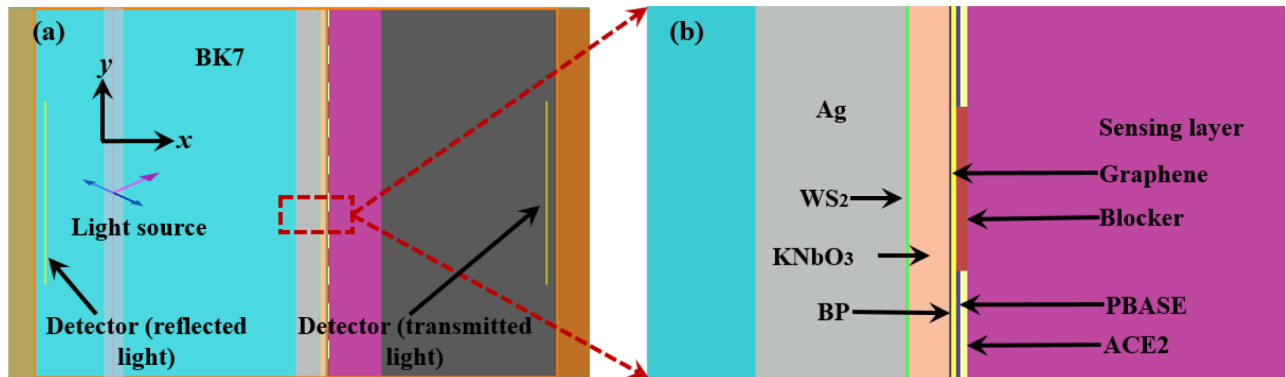
$$S = \frac{\Delta\theta_r}{\Delta n_s}, \tag{7}$$

where $\Delta\theta_r$ is the change in resonance angle θ_r for Δn_s change in n_s. On the other hand, FoM is defined as [74]

$$\text{FoM} = \frac{S}{\Delta\theta_{i,(1/2)}}, \tag{8}$$

where $\Delta\theta_{i,(1/2)}$ is the full-width of θ_i at the half-maximum points on the R-profile.

Fig 4. (a) Simulation setup in the *xy* plane and (b) Material layers in the simulation domain.

3.3 Simulation method

In this work, we solve 2-D full-field Maxwell's equations using the FDTD method to calculate the interaction of the incident light with the sensor structure and determine the SPR dynamics. For this purpose, we use Lumerical FDTD Solutions. Since the structure is invariant in the *z*-direction, both 3-D and 2-D models produce the same results [75]. The 2-D simulation setup of the proposed sensor is shown in Fig 4. Fig 4 also shows the positions of the incident light source and reflection and transmission detection planes. The simulation area is 1600 nm in the *x*-direction and 1000 nm in the *y*-direction. We apply a non-uniform meshing technique with ultra-fine mesh grids in FDTD simulations to limit the overall error to <0.05%. Furthermore, the simulation boundaries in the *x*-direction are PML, while Bloch boundaries terminate those in the *y*-direction. The incident light is a plane wave with a 633 nm wavelength and TM polarization. The incident light source is located at 750 nm from the BK7–Ag interface, whereas the reflected light intensity is recorded at 775 nm from the same interface.

For total internal reflection, the incidence angle θ_i must be greater than the critical angle (θ_c). The total light absorption of the sensor is $A = 1 - T - R$, where T is the transmission coefficient. Here, as the incident light will experience an attenuated total reflection, $T = 0$; therefore, we can write $A = 1 - R$. When SPs are excited at the resonance incident angle, R drops sharply. In this work, we vary θ_i from 55° to 85°, with a step size of 0.099° to calculate the R-profile for mass level S-protein concentrations. Additionally, for ultra-low-level SARS-CoV-2 detection, we vary θ_i from 65.30° to 65.60°, with a step size of 0.00149°.

4 Results and discussion

4.1 Detection approach and limit of detection

As the SARS-CoV-2 S-protein concentration in PBS changes, the sensing layer experiences a refractive index variation. Consequently, the SP wave vector changes, eventually changing θ_r. Fig 5(a) shows R-profiles of the proposed sensor as a function of θ_i for different SARS-CoV-2 S-protein concentrations. When the sensing layer contains only the PBS, without any SARS-CoV-2 S-protein, θ_r is 65.44°. The change of R-profile depends on the refractive indices of the buffer layer, such as the PBS, and the target molecule, such as the S-protein concentration. When the S-protein concentration is 1 fM, θ_r shifts to 65.445° and 65.450° for 100-μL or 200-μL PBS, respectively. Thus, the change in θ_r, i.e., $\Delta\theta_r$, is 0.005° and 0.01° when 1 fM SARS-CoV-2 S-protein is present in 100-μL and 200-μL PBS, respectively, as shown in Fig 5(b). R_{min}
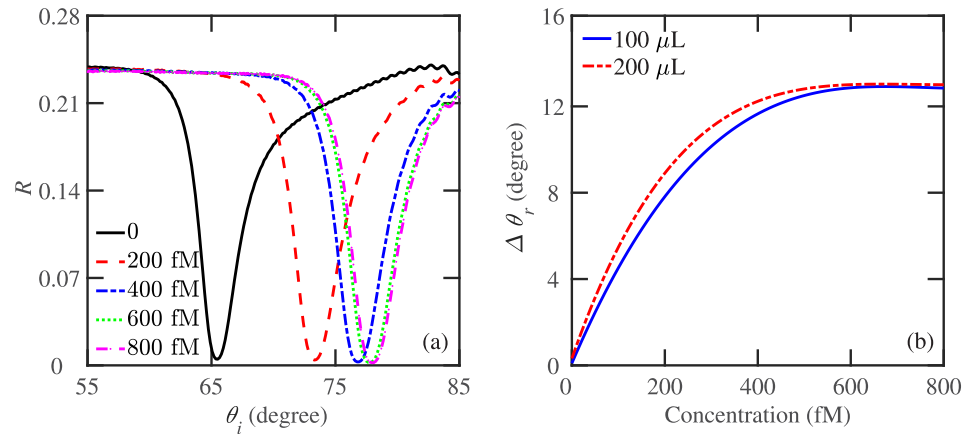
Fig 5. (a) *R*-profile of the proposed graphene SPR sensor for different SARS-CoV-2 S-protein concentrations as a function of θ_i. In this case, SARS-CoV-2 S-proteins are added to 100-μL PBS solution. (b) $\Delta\theta_r$ against SARS-CoV-2 S-protein concentration for 100-μL and 200-μL PBS solution.

also decreases slightly when the S-protein concentration increases due to the enhanced absorption of the incident light.

Fig 5(b) shows $\Delta\theta_r = \theta_{r(\text{PBS+ACE2+S-protein})} - \theta_{r(\text{PBS+ACE2})}$ calculated from the *R*-profiles as the S-protein concentration varies for 100- and 200-μL PBS solutions. We note that $\Delta\theta_r$ increases significantly with the S-protein concentration. Increasing the S-protein concentration increases the sensing layer refractive index, enhancing light absorption. As a result, the $\Delta\theta_r$ shifts more. However, $\Delta\theta_r$ does not vary noticeably when S-protein concentration is $\gtrsim$ 600 fM in 100-μL PBS solution, as shown in Fig 5(b). Similarly, $\Delta\theta_r$ shows a saturating behavior when the S-protein concentration is $\gtrsim$ 500 fM in 200-μL PBS solution. A similar tendency has been observed in the literature, showing $\Delta\theta_r$ saturation behavior when the S-protein concentration is >104 copies/ml [20]. Now, the refractive index increases more with the S-protein concentration in the 200-μL PBS solution than in the 100-μL PBS solution, as shown in Fig 3. Therefore, the saturation behavior is manifested at a smaller S-protein concentration in the 200-μL PBS solution than in the 100-μL PBS solution. The maximum θ_r shifts are $\Delta\theta_{r(\text{max})}$ = 12.56° and 12.72° for 100-μL or 200-μL PBS solutions, respectively.

To detect the SARS-CoV-2 S-protein, $\Delta\theta_r$ values are used. As S-proteins incrementally adsorb to the sensor surface, θ_r keeps shifting to greater values until it reaches the maximum [76]. S-proteins are detected when $\Delta\theta_r$ > 0. Now, LoD is determined from the minimum S-protein concentration for which a non-zero $\Delta\theta_r$ is registered. The proposed sensor shows $\Delta\theta_r$ > 0 even when the SARS-CoV-2 S-protein concentration is only 1 fM, enabling the proposed sensor to detect as low as 1 fM SARS-CoV-2 S-protein.

The LoD of a sensor is an essential parameter, especially when detecting a critical pathogen like SARS-CoV-2. In Table 2, we compare the LoD of the proposed sensor with some recently proposed sensors that use plasmonic techniques to detect the SARS-CoV-2 S-protein. The proposed sensor shows a much smaller LoD than that reported by these state-of-the-art sensors. We note that the plasmonic meta-sensor of Ref. [19] shows an LoD of $\sim$4.2 fM, relatively close to that obtained from the proposed sensor in this work. However, the meta-sensor operates in the THz range and is bulky. The meta-sensor also does not work for the entire range of the S-protein concentration.

Table 2. Comparisons of LoD of the proposed sensor with different recently proposed sensors for SARS-CoV-2 S-protein detection.

| Sensor device	Assay components	LoD
MRT-PCR [77]	SARS-CoV-2	5 μM
dd-PCR [78]	SARS-CoV-2	0.00187 ng
RT-LAMP [79]	SARS-CoV-2	0.025 μg/μl
FET biosensor [20]	SARS-CoV-2	1 fg/ml
Meta-sensor [19]	Gold NPs, SARS-CoV-2	$\sim$4.2 fM
Photo-thermal biosensor [4]	Gold NPs, SARS-CoV-2	0.22 pM
NIR biosensor [3]	ITO, tellurene, MoS_2-COOH, SARS-CoV-2	$\sim$301.67 nM
LSPR biosensor [80]	Au nano-spikes in opto-microfluidic chip	$\sim$0.5 pM
This work	Graphene, PBASE, ACE2, SARS-CoV-2	1 fM

https://doi.org/10.1371/journal.pone.0284812.t002

4.2 Sensor resolution and binding affinity

In Fig 6(a), we show the proposed sensor's resolution (SR) as a function of the S-protein concentration. The resolution of a sensor can be determined by [81]

$$\text{SR} = \Delta n_s \, \frac{\Delta\theta_{r(\min)}}{\Delta\theta_{r(\max)}}, \tag{9}$$

where $\Delta\theta_{r(\min)}$ is the minimum spectrum resolution, and $\Delta\theta_{r(\max)}$ is the maximum θ_r shift. The maximum SR is 0.25×10^{-5} RIU when the S-protein concentration is 800 fM for 100-μL PBS solution. When the S-protein concentration is 1 fM, the SR is 0.015×10^{-5} RIU and 0.016×10^{-5} RIU for 100-μL and 200-μL PBS solutions, respectively. The SR of the proposed sensor signifies its ability to detect SARS-CoV-2 S-protein in minute index variations such as on the order of 10^{-5} RIU, which is significant compared to the recently reported SR values in the literature [81–83].

In an SPR sensor, a flow channel is typically used to inject an aqueous solution to the sensor surface [84]. In our proposed sensor, the PBS solution containing SARS-CoV-2 can be injected into the channel where ACE2 antibodies are immobilized on the graphene surface. SARS-CoV-2 S-proteins must bind to ACE2 antibodies on the sensor surface to change the refractive
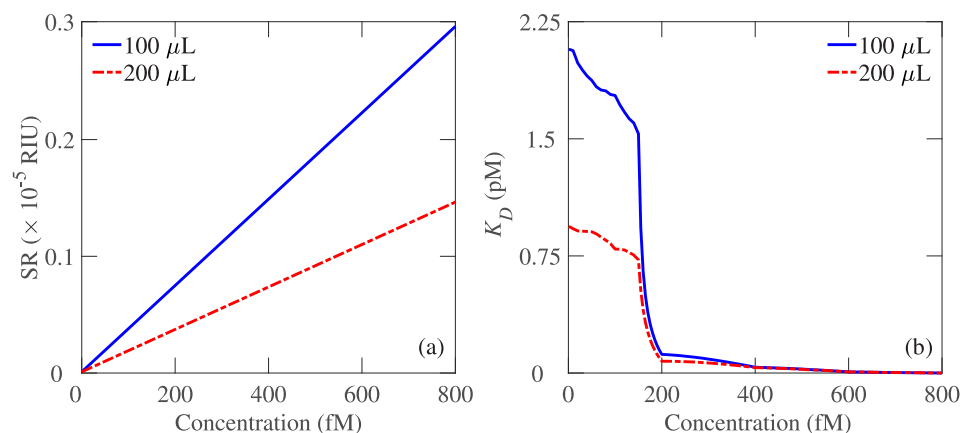
Fig 6. (a) SR and (b) K_D as a function of S-protein concentration of the proposed graphene SPR sensor for 100-μL and 200-μL PBS solutions.

https://doi.org/10.1371/journal.pone.0284812.g006

index of the sensing layer. The binding between the immobilized ACE2 antibodies and S-proteins is denoted by the association constant (K_A) or the dissociation constant (K_D), where $K_D = 1/K_A$. We can derive an expression for K_D using the Langmuir model [16]

$$K_D = C\left[\frac{\Delta\theta_{r(\max)}}{\Delta\theta_r} - 1\right].\qquad(10)$$

Langmuir model is a ligand binding model to justify the affinity of analyte-antibody bindings [85]. Generally, the K_D value for proteins on an SPR sensor is < 10 nM [86]. The K_D value should be as small as possible because a smaller K_D value represents a greater binding affinity of the sensor to its target element. Fig 6(b) shows K_D of the proposed sensor as a function of the S-protein concentration. We note that the binding affinity between ACE2 and S-protein increases with the S-protein concentration. The K_D value is smaller with the 200-μL PBS solution than that with the 100-μL PBS solution due to the increasing number of S-proteins in greater PBS volume enhancing the chances of binding between ACE2 and S-proteins. We note that the proposed sensor shows a smaller K_D value compared to recent reports on k_D values in the literature [86].

4.3 Sensing performance

The selectivity of the proposed graphene SPR SARS-CoV-2 sensor can be determined from the change in θ_r as the S-protein concentration changes [16]. Fig 5(b) shows $\Delta\theta_r$ for different S-protein concentrations for two PBS solutions. $\Delta\theta_r$ increases with the S-protein concentration, with the increase more significant for the 200-μL PBS solution, signifying that the proposed sensor has an affinity toward S-proteins [48]. As $\Delta\theta_r$ sensitively changes with the S-protein concentration, the proposed sensor is highly selective of the S-protein. The proposed sensor shows comparatively greater selectivity compared to recent reports in the literature [16, 87, 88].

Fig 7(a) shows the sensitivity of the proposed graphene SPR sensor as a function of the SARS-CoV-2 S-protein concentration. As the sensitivity depends on the change of θ_r and increasing S-protein concentration shows a more significant change in θ_r, we find that the sensitivity increases as the S-protein concentration increases. Also, the 200-μL PBS solution shows
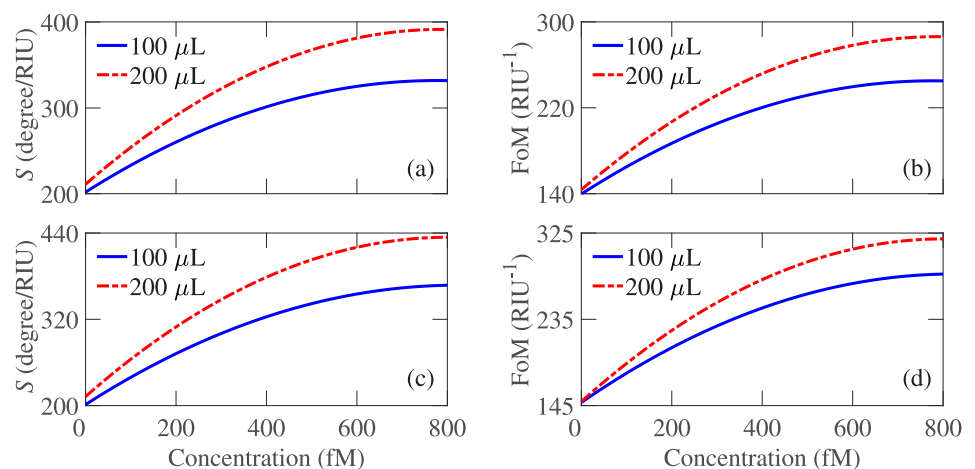
Fig 7. (a) S and (b) FoM using BP and (c) S and (d) FoM using BlueP as a function of S-protein concentration of the proposed graphene SPR sensor for 100-μL and 200-μL PBS solutions.

https://doi.org/10.1371/journal.pone.0284812.g007

greater sensitivity than the 100-μL PBS solution because the S-protein number increases with PBS solution volume, which increases $\Delta\theta_r$. When the S-protein concentration is 1 fM, $S = 201$ degrees/RIU and 210 degrees/RIU for 100-μL and 200-μL PBS solutions, respectively. Furthermore, the proposed sensor shows the maximum sensitivity of 371 degrees/RIU when the S-protein concentration is 800 fM for 200-μL PBS solution.

The FoM of the proposed sensor has been presented in Fig 7(b) as a function of the S-protein concentration. We note that FoM increases with the increase of S-protein concentration. When the S-protein concentration is 800 fM, the FoM is maximum with values of 233 RIU^{-1} and 275 RIU^{-1} for 100-μL and 200-μL PBS solutions, respectively. Moreover, 1 fM S-protein concentration shows 140 RIU^{-1} and 148 RIU^{-1} FoM for 100-μL and 200-μL PBS solutions, respectively. As the increasing S-protein concentration raises n_s, θ_r increases. In addition, as the FoM is directly related to the sensitivity according to Eq (11), it increases when the sensitivity increases.

Fig 7(c) shows the sensitivity of the proposed sensor as a function of the SARS-CoV-2 S-protein concentration using BlueP instead of BP. The sensitivity increases as the S-protein concentration increases. The sensitivity with BlueP is comparable to that with BP at the ultra-low-level S-protein concentration. However, when the S-protein concentration increases, the sensor with BlueP shows greater sensitivity than with BP. When the S-protein concentration is 800 fM, the sensitivity for the sensor with BlueP is 365 degrees/RIU and 435 degrees/RIU for 100-μL and 200-μL PBS solutions, respectively, $\sim$10% greater than the sensor with BP.

Fig 7(d) shows the FoM as a function of the SARS-CoV-2 S-protein concentration using BlueP instead of BP. BlueP shows greater FoM than BP for ultra-low-level and mass-level S-protein concentrations. For example, when the S-protein concentration is 1 fM, FoMs for the sensor with BP are 152 RIU^{-1} and 153 RIU^{-1} for 100-μL and 200-μL PBS solutions, respectively, $\sim$4% greater than the sensor with BP. Furthermore, when the S-protein concentration is 800 fM, FoMs for the sensor with BlueP are 282 RIU^{-1} and 318 RIU^{-1} for 100-μL and 200-μL PBS solutions, respectively, $\sim$15% greater than the sensor with BP. The enhancement in FoM with the BlueP can be attributed to its narrower R spectrum than BP.

As the proposed sensor has several layers of different refractive indices, calculating the dispersion relation is numerically challenging. This work analyzes the dispersion relations using the radiative mode [89]. The in-plane wave vector can be given by [89]

$$\beta = \frac{\omega\sqrt{\varepsilon_{\text{prism}}}}{c}\sin\theta_r, \tag{11}$$

where $\varepsilon_{\text{prism}}$ is the dielectric constant of the prism, ω is the angular frequency, and c is the speed of light in vacuum. Fig 8(a) shows the dispersion relation of the proposed sensor. We compute the reflectivity of the proposed sensor as a function of the frequency and θ_i. The frequency is varied from 4.2827×10^{14} Hz to 5.2138×10^{14} Hz and θ_i is varied from 55° to 85°. We find that the dispersion curve moves away from the air light-line. We note that at >630 nm wavelength ($\omega = 2.9 \times 10^{15}$ Hz), dispersion relations for both 100-μL and 200-μL PBS solutions move farther from the light line.

On the other hand, SPPs suffer damping in metal, decreasing the propagation length significantly [90]. Mainly, damping depends on the dielectric constant of metal at the oscillation frequency of SPPs. Losses may also occur due to the coupling of SPPs to radiation modes. Propagation loss depends on the sensing layer's dielectric constant [91]. The propagation
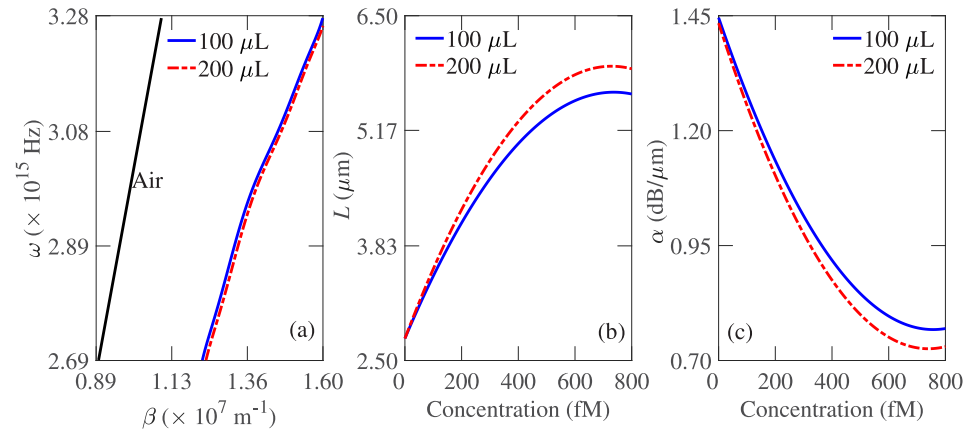
Fig 8. (a) Dispersion relations of the proposed sensor when the S-protein concentration is 1 fM using BP. The most left straight line is the light line, (b) Propagation length, and (c) Propagation loss of the proposed sensor as a function of the SARS-CoV-2 S-protein concentration for 100-μL and 200-μL PBS solutions.

length can be defined by [92]

$$L = \frac{1}{\Delta\theta_{i,(1/2)} n_p \frac{\omega}{c} cos\theta_r}, \tag{12}$$

where n_p is the refractive index of the prism. Also, the propagation loss can be calculated by [92]

$$\alpha = [-10\log(1/e)]/L \approx 4.343/L. \tag{13}$$

Fig 8(b) shows that the propagation length increases with the SARS-CoV-2 S-protein concentration. Also, the 200-μm PBS solution shows a greater propagation length than the 100-μm PBS solution since the sensing layer's refractive index increases with the S-protein concentration, enhancing light confinement. Our proposed sensor shows a small propagation length <10 μm, which is a short-range SPP. As a result, the propagation loss decreases with the S-protein concentration, as shown in Fig 8(c). When the propagation length increases from 2.62 μm to 5.84 μm, the propagation loss decreases from 1.44 dB/μm to 0.72 dB/μm for 200-μm PBS solution. Compared to the existing literature, the proposed sensor performs better in decreasing the loss [92].

The proposed sensor's sensitivity and FoM performances are significantly better than the state-of-the-art optical sensors. We compare the sensitivity and FoM of the proposed sensor in Table 3 with some recently reported sensors. We have compared the minimum sensitivity and FoM achievable from the proposed sensor at the LoD with those reported in the literature. We have considered the sensors for comparison that specifically use similar 2-D materials. The compared sensors also operate at 633 nm incident wavelength and report results for a sample of ~ 1.3349 refractive index, which is the same n_s value of this work at 1 fM S-protein concentration in 200-μL PBS solution.

5 Conclusion

Tackling the COVID-19 pandemic requires rapid, low-cost, and sensitive detection of ultra-low-level SARS-CoV-2. The proposed sensor will detect SARS-CoV-2 in real time without

Table 3. Performance comparison of our proposed sensor with different recently proposed sensors.

Sensor configuration	S (degrees/RIU)	FoM (RIU^{-1})
Prism /TiO$_2$ /SiO$_2$ /Ag /MoS$_2$ /Graphene /Sensing layer [93]	98	88.89
Prism /ZnO /Ag /BaTiO$_3$ /Graphene /Sensing layer [94]	157	71
Prism /Au /PtSe$_2$ /Graphene /Sensing layer [95]	154	–
Prism /Ag /PtSe$_2$ /Sensing layer [96]	162	15
Prism /Al /Au /Graphene /WSe$_2$ /Sensing layer [97]	164	–
This work (BP/BlueP)	210/210	148/153

https://doi.org/10.1371/journal.pone.0284812.t003

requiring any label or complicated sample preparation. The proposed sensor shows a significant change in the SPR resonance when the SARS-CoV-2 concentration varies even at the femtomolar level, and hence is suitable for sensitive ultra-low-level SARS-CoV-2 detection and early detection of COVID-19. The proposed sensor's sensitivity and FoM performances are significantly better than the state-of-the-art optical sensors. The proposed sensor also shows much stronger binding kinetics with the sensor surface than recent reports in the literature. The results and analysis confirm that the proposed sensor is promising for SARS-CoV-2 detection and may find applications in detecting other biochemical and biological analytes.

Author Contributions

Conceptualization: Md. Mahbub Hossain, Muhammad Anisuzzaman Talukder.

Formal analysis: Md. Mahbub Hossain, Muhammad Anisuzzaman Talukder.

Supervision: Muhammad Anisuzzaman Talukder.

Validation: Md. Mahbub Hossain.

Writing – original draft: Md. Mahbub Hossain.

Writing – review & editing: Muhammad Anisuzzaman Talukder.

References

1. Kang S, Yang M, Hong Z, Zhang L, Huang Z, Chen X, et al. Crystal structure of SARS-CoV-2 nucleocapsid protein RNA binding domain reveals potential unique drug targeting sites. Acta Pharmaceutica Sinica B. 2020; 10(7):1228–1238. https://doi.org/10.1016/j.apsb.2020.04.009 PMID: 32363136

2. Mauriz E. Recent progress in plasmonic biosensing schemes for virus detection. Sensors. 2020; 20 (17):4745. https://doi.org/10.3390/s20174745 PMID: 32842601

3. Peng X, Zhou Y, Nie K, Zhou F, Yuan Y, Song J, et al. Promising near-infrared plasmonic biosensor employed for specific detection of SARS-CoV-2 and its spike glycoprotein. New Journal of Physics. 2020; 22(10):103046. https://doi.org/10.1088/1367-2630/abbe53

4. Qiu G, Gai Z, Tao Y, Schmitt J, Kullak-Ublick GA, Wang J. Dual-functional plasmonic photothermal biosensors for highly accurate severe acute respiratory syndrome coronavirus 2 detection. ACS Nano. 2020; 14(5):5268–5277. https://doi.org/10.1021/acsnano.0c02439 PMID: 32281785

5. Park GS, Ku K, Baek SH, Kim SJ, Kim SI, Kim BT, et al. Development of reverse transcription loop-mediated isothermal amplification assays targeting severe acute respiratory syndrome coronavirus 2 (SARS-CoV-2). The Journal of Molecular Diagnostics. 2020; 22(6):729–735. https://doi.org/10.1016/j.jmoldx.2020.03.006 PMID: 32276051

6. Xiong Z, Xiaoxia W, Limei H, Ting C, Licheng W, Huan L, et al. Reverse transcription loop-mediated isothermal amplification combined with nanoparticles-based biosensor for diagnosis of COVID-19. MedRxiv. 2020;.

7. Hossein H, Ali KM, Hosseini M, Sarveazad A, Safari S, Yousefifard M. Value of chest computed tomography scan in diagnosis of COVID-19; a systematic review and meta-analysis. Clinical and Translational Imaging. 2020; p. 1–13.

8. Egger M, Bundschuh C, Wiesinger K, Gabriel C, Clodi M, Mueller T, et al. Comparison of the Elecsys® Anti-SARS-CoV-2 immunoassay with the EDI™ enzyme linked immunosorbent assays for the detection of SARS-CoV-2 antibodies in human plasma. Clinica Chimica Acta. 2020; 509:18–21. https://doi.org/10.1016/j.cca.2020.05.049 PMID: 32485155

9. Kumar PK. Monitoring intact viruses using aptamers. Biosensors. 2016; 6(3):40. https://doi.org/10.3390/bios6030040 PMID: 27527230

10. Fang Y, Zhang H, Xie J, Lin M, Ying L, Pang P, et al. Sensitivity of chest CT for COVID-19: comparison to RT-PCR. Radiology. 2020; 296(2):E115–E117. https://doi.org/10.1148/radiol.2020200432 PMID: 32073353

11. Chou Chau YF, Chen KH, Chiang HP, Lim CM, Huang HJ, Lai CH, et al. Fabrication and characterization of a metallic–dielectric nanorod array by nanosphere lithography for plasmonic sensing application. Nanomaterials. 2019; 9(12):1691. https://doi.org/10.3390/nano9121691 PMID: 31779222

12. Chou Chau YF, Chou Chao CT, Huang HJ, Kooh MRR, Kumara N, Lim CM, et al. Perfect dual-band absorber based on plasmonic effect with the cross-hair/nanorod combination. Nanomaterials. 2020; 10(3):493. https://doi.org/10.3390/nano10030493 PMID: 32182902

13. Chou Chau YF, Ming TY, Chou Chao CT, Thotagamuge R, Kooh MRR, Huang HJ, et al. Significantly enhanced coupling effect and gap plasmon resonance in a MIM-cavity based sensing structure. Scientific Reports. 2021; 11(1):1–17. https://doi.org/10.1038/s41598-021-98001-z

14. Chou Chau YF, Chou Chao CT, Huang HJ, Kooh MRR, Kumara NTRN, Lim CM, et al. Ultrawide bandgap and high sensitivity of a plasmonic metal-insulator-metal waveguide filter with cavity and baffles. Nanomaterials. 2020; 10(10):2030. https://doi.org/10.3390/nano10102030 PMID: 33076338

15. Chao CTC, Chau YFC, Mahadi AH, Kooh MRR, Kumara N, Chiang HP, et al. Plasmonic refractive index sensor based on the combination of rectangular and circular resonators including baffles. Chinese Journal of Physics. 2021; 71:286–299. https://doi.org/10.1016/j.cjph.2021.02.006

16. Omar NAS, Fen YW, Abdullah J, Sadrolhosseini AR, Mustapha Kamil Y, Fauzi NM, et al. Quantitative and selective surface plasmon resonance response based on a reduced graphene oxide–polyamidoamine nanocomposite for detection of dengue virus E-proteins. Nanomaterials. 2020; 10(3):569. https://doi.org/10.3390/nano10030569 PMID: 32245185

17. Omair Z, Talukder MA. Sensitivity analysis of gold nanorod biosensors for single molecule detection. Plasmonics. 2019; 14(6):1611–1619. https://doi.org/10.1007/s11468-019-00946-5

18. Lee JH, Kim BC, Oh BK, Choi JW. Highly sensitive localized surface plasmon resonance immunosensor for label-free detection of HIV-1. Nanomedicine: Nanotechnology, Biology and Medicine. 2013; 9(7):1018–1026. https://doi.org/10.1016/j.nano.2013.03.005 PMID: 23506952

19. Ahmadivand A, Gerislioglu B, Ramezani Z, Kaushik A, Manickam P, Ghoreishi SA. Femtomolar-level detection of SARS-CoV-2 spike proteins using toroidal plasmonic metasensors. arXiv preprint arXiv:200608536. 2020;.

20. Giwan S, Geonhee L, Mi Jeong K, Seung-Hwa B, Minsuk C, Keun BK, et al. Rapid detection of COVID-19 causative virus (SARS-CoV-2) in human nasopharyngeal swab specimens using field-effect transistor-based biosensor. ACS Nano. 2020; 14(4):5135–5142. https://doi.org/10.1021/acsnano.0c02823

21. Parihar A, Khan R, Kumar A, Kaushik AK, Gohel H. Computational Approaches for Novel Therapeutic and Diagnostic Designing to Mitigate SARS-CoV2 Infection: Revolutionary Strategies to Combat Pandemics. Elsevier; 2022.

22. Khan R, Parihar A, Kaushik AK, Kumar A. Advanced Biosensors for Virus Detection: Smart Diagnostics to Combat SARS-CoV-2. Academic Press; 2022.

23. Singhal A, Parihar A, Kumar N, Khan R. High throughput molecularly imprinted polymers based electrochemical nanosensors for point-of-care diagnostics of COVID-19. Materials Letters. 2022; 306:130898. https://doi.org/10.1016/j.matlet.2021.130898 PMID: 34566219

24. Sadique MA, Yadav S, Ranjan P, Khan R, Khan F, Kumar A, et al. Highly Sensitive Electrochemical Immunosensor Platforms for Dual Detection of SARS-CoV-2 Antigen and Antibody based on Gold Nanoparticle Functionalized Graphene Oxide Nanocomposites. ACS Applied Bio Materials. 2022;. https://doi.org/10.1021/acsabm.2c00301 PMID: 35522141

25. Yadav S, Sadique MA, Ranjan P, Khan R, Sathish N, Srivastava AK. Polydopamine decorated MoS2 nanosheet based electrochemical immunosensor for sensitive detection of SARS-CoV-2 nucleocapsid protein in clinical samples. Journal of Materials Chemistry B. 2022;. https://doi.org/10.1039/D2TB01409B PMID: 36197135

26. Wrapp D, Wang N, Corbett KS, Goldsmith JA, Hsieh CL, Abiona O, et al. Cryo-EM structure of the 2019-nCoV spike in the prefusion conformation. Science. 2020; 367(6483):1260–1263. https://doi.org/10.1126/science.abb2507 PMID: 32075877

27. Priyadarsini S, Mohanty S, Mukherjee S, Basu S, Mishra M. Graphene and graphene oxide as nanomaterials for medicine and biology application. Journal of Nanostructure in Chemistry. 2018; 8(2):123–137. https://doi.org/10.1007/s40097-018-0265-6

28. Maurya J, Prajapati Y. A comparative study of different metal and prism in the surface plasmon resonance biosensor having MoS_2-graphene. Optical and Quantum Electronics. 2016; 48(5):280. https://doi.org/10.1007/s11082-016-0562-6

29. Ahmadivand A, Gerislioglu B, Ahuja R, Mishra YK. Terahertz plasmonics: The rise of toroidal metadevices towards immunobiosensings. Materials Today. 2020; 32:108–130. https://doi.org/10.1016/j.mattod.2019.08.002

30. Ahmadivand A, Gerislioglu B, Noe GT, Mishra YK. Gated graphene enabled tunable charge–current configurations in hybrid plasmonic metamaterials. ACS Applied Electronic Materials. 2019; 1(5):637–641. https://doi.org/10.1021/acsaelm.9b00035

31. Lin C, Chen S. Design of highly sensitive guided-wave surface plasmon resonance biosensor with deep dip using genetic algorithm. Optics Communications. 2019; 445:155–160. https://doi.org/10.1016/j.optcom.2019.04.035

32. Li K, Li L, Xu N, Peng X, Zhou Y, Yuan Y, et al. Ultrasensitive Surface Plasmon Resonance Biosensor Using Blue Phosphorus–Graphene Architecture. Sensors. 2020; 20(11):3326. https://doi.org/10.3390/s20113326 PMID: 32545230

33. Feng Y, Liu Y, Teng J. Design of an ultra-sensitive SPR biosensor based on a graphene-MoS 2 hybrid structure with a MgF_2 prism. Applied Optics. 2018; 57(14):3639–3644. https://doi.org/10.1364/AO.57.003639 PMID: 29791325

34. Chau YF, Jiang ZH, Li HY, Lin GM, Wu FL, Lin WH. Localized resonance of composite core-shell nanospheres, nanobars and nanospherical chains. Progress In Electromagnetics Research B. 2011; 28:183–199. https://doi.org/10.2528/PIERB10102705

35. Chau YF, Yeh HH, Tsai D. Surface plasmon resonances effects on different patterns of solid-silver and silver-shell nanocylindrical pairs. Journal of Electromagnetic Waves and Applications. 2010; 24(8-9):1005–1014. https://doi.org/10.1163/156939310791586098

36. Chau YFC, Jiang JC, Chao CTC, Chiang HP, Lim CM. Manipulating near field enhancement and optical spectrum in a pair-array of the cavity resonance based plasmonic nanoantennas. Journal of Physics D: Applied Physics. 2016; 49(47):475102. https://doi.org/10.1088/0022-3727/49/47/475102

37. Xue T, Liang W, Li Y, Sun Y, Xiang Y, Zhang Y, et al. Ultrasensitive detection of miRNA with an antimonene-based surface plasmon resonance sensor. Nature Communications. 2019; 10(1):1–9. https://doi.org/10.1038/s41467-018-07947-8 PMID: 30604756

38. Georgakilas V, Otyepka M, Bourlinos AB, Chandra V, Kim N, Kemp KC, et al. Functionalization of graphene: covalent and non-covalent approaches, derivatives and applications. Chemical Reviews. 2012; 112(11):6156–6214. https://doi.org/10.1021/cr3000412 PMID: 23009634

39. Huang Y, Dong X, Shi Y, Li CM, Li LJ, Chen P. Nanoelectronic biosensors based on CVD grown graphene. Nanoscale. 2010; 2(8):1485–1488. https://doi.org/10.1039/c0nr00142b PMID: 20820739

40. Roujian L, Xiang Z, Juan L, Peihua N, Bo Y, Honglong W, et al. Genomic characterisation and epidemiology of 2019 novel coronavirus: implications for virus origins and receptor binding. The Lancet. 2020; 395(10224):565–574. https://doi.org/10.1016/S0140-6736(20)30251-8

41. Shen S, Tan TH, Tan YJ. Expression, glycosylation, and modification of the spike (S) glycoprotein of SARS CoV. Glycovirology Protocols. 2007; p. 127–135. https://doi.org/10.1007/978-1-59745-393-6_9 PMID: 17502675

42. Ou X, Liu Y, Lei X, Li P, Mi D, Ren L, et al. Characterization of spike glycoprotein of SARS-CoV-2 on virus entry and its immune cross-reactivity with SARS-CoV. Nature Communications. 2020; 11(1):1–12. https://doi.org/10.1038/s41467-020-15562-9 PMID: 32221306

43. Peterlinz KA, Georgiadis RM, Herne TM, Tarlov MJ. Observation of hybridization and dehybridization of thiol-tethered DNA using two-color surface plasmon resonance spectroscopy. Journal of the American Chemical Society. 1997; 119(14):3401–3402. https://doi.org/10.1021/ja964326c

44. Reitmeier R, Sivertz V, Tartar H. Some properties of monoethanolamine and its aqueous solutions. Journal of the American Chemical Society. 1940; 62(8):1943–1944. https://doi.org/10.1021/ja01865a009

45. Kim DH, Oh HG, Park WH, Jeon DC, Lim KM, Kim HJ, et al. Detection of alpha-fetoprotein in hepatocellular carcinoma patient plasma with graphene field-effect transistor. Sensors. 2018; 18(11):4032. https://doi.org/10.3390/s18114032 PMID: 30463232

46. Perchetti GA, Huang ML, Peddu V, Jerome KR, Greninger AL. Stability of SARS-CoV-2 in PBS for molecular detection. Journal of Clinical Microbiology. 2020;. https://doi.org/10.1128/JCM.01094-20 PMID: 32414839

47. Hoang VT, Stępniewski G, Czarnecka KH, Kasztelanic R, Long VC, Xuan KD, et al. Optical properties of buffers and cell culture media for optofluidic and sensing applications. Applied Sciences. 2019; 9 (6):1145. https://doi.org/10.3390/app9061145

48. Hossain MM, Talukder MA. Gate-controlled graphene surface plasmon resonance glucose sensor. Optics Communications. 2021; p. 126994. https://doi.org/10.1016/j.optcom.2021.126994

49. Wu C, Zhou X, Wei J. Localized surface plasmon resonance of silver nano-triangles synthesized by a versatile solution reaction. Nanoscale Research Letters. 2015; 10(1):1–6. https://doi.org/10.1186/1556-276X-10-1

50. Yguerabide J, Yguerabide EE. Light-scattering submicroscopic particles as highly fluorescent analogs and their use as tracer labels in clinical and biological applications: II. Experimental characterization. Analytical Biochemistry. 1998; 262(2):157–176. https://doi.org/10.1006/abio.1998.2759 PMID: 9750129

51. Holm RH, Solomon EI, Majumdar A, Tenderholt A. Comparative molecular chemistry of molybdenum and tungsten and its relation to hydroxylase and oxotransferase enzymes. Coordination Chemistry Reviews. 2011; 255(9-10):993–1015. https://doi.org/10.1016/j.ccr.2010.10.017

52. Wang M, Huo Y, Jiang S, Zhang C, Yang C, Ning T, et al. Theoretical design of a surface plasmon resonance sensor with high sensitivity and high resolution based on graphene–WS_2 hybrid nanostructures and Au–Ag bimetallic film. RSC Advances. 2017; 7(75):47177–47182. https://doi.org/10.1039/C7RA08380G

53. Zhao X, Huang T, Ping PS, Wu X, Huang P, Pan J, et al. Sensitivity enhancement in surface plasmon resonance biochemical sensor based on transition metal dichalcogenides/graphene heterostructure. Sensors. 2018; 18(7):2056. https://doi.org/10.3390/s18072056 PMID: 29954134

54. Desu SB, Payne DA. Interfacial segregation in perovskites: III, microstructure and electrical properties. Journal of the American Ceramic Society. 1990; 73(11):3407–3415. https://doi.org/10.1111/j.1151-2916.1990.tb06468.x

55. Wu L, Guo J, Wang Q, Lu S, Dai X, Xiang Y, et al. Sensitivity enhancement by using few-layer black phosphorus-graphene/TMDCs heterostructure in surface plasmon resonance biochemical sensor. Sensors and Actuators B: Chemical. 2017; 249:542–548. https://doi.org/10.1016/j.snb.2017.04.110

56. Elshorbagy MH, Cuadrado A, Alda J. High-sensitivity integrated devices based on surface plasmon resonance for sensing applications. Photonics Research. 2017; 5(6):654–661. https://doi.org/10.1364/PRJ.5.000654

57. Ouyang Q, Zeng S, Jiang L, Hong L, Xu G, Dinh XQ, et al. Sensitivity enhancement of transition metal dichalcogenides/silicon nanostructure-based surface plasmon resonance biosensor. Scientific Reports. 2016; 6(1):1–13. https://doi.org/10.1038/srep28190 PMID: 27305974

58. Sun P, Wang M, Liu L, Jiao L, Du W, Xia F, et al. Sensitivity enhancement of surface plasmon resonance biosensor based on graphene and barium titanate layers. Applied Surface Science. 2019; 475:342–347. https://doi.org/10.1016/j.apsusc.2018.12.283

59. Hossain MM, Talukder MA. Optical Magnetism in Surface Plasmon Resonance–Based Sensors for Enhanced Performance. Plasmonics. 2021; 16(2):581–588. https://doi.org/10.1007/s11468-020-01316-2

60. Ghosh B, Nahas S, Bhowmick S, Agarwal A. Electric field induced gap modification in ultra-thin blue phosphorus. Physical Review B. 2015; 91(11):115433. https://doi.org/10.1103/PhysRevB.91.115433

61. Maharana PK, Srivastava T, Jha R. On the performance of highly sensitive and accurate graphene-on-aluminum and silicon-based SPR biosensor for visible and near infrared. Plasmonics. 2014; 9(5):1113–1120. https://doi.org/10.1007/s11468-014-9721-4

62. Jung GH, Yoo S, Park QH. Measuring the optical permittivity of two-dimensional materials without a priori knowledge of electronic transitions. Nanophotonics. 2018; 8(2):263–270. https://doi.org/10.1515/nanoph-2018-0120

63. Umemura N, Yoshida K, Kato K. Phase-matching properties of $KNbO_3$ in the mid-infrared. Applied Optics. 1999; 38(6):991–994. https://doi.org/10.1364/AO.38.000991 PMID: 18305704

64. Wang X, Lan S. Optical properties of black phosphorus. Advances in Optics and photonics. 2016; 8 (4):618–655. https://doi.org/10.1364/AOP.8.000618

65. Mogulkoc Y, Modarresi M, Mogulkoc A, Ciftci Y. Electronic and optical properties of bilayer blue phosphorus. Computational Materials Science. 2016; 124:23–29. https://doi.org/10.1016/j.commatsci.2016.07.015

66. Bruna M, Borini S. Optical constants of graphene layers in the visible range. Applied Physics Letters. 2009; 94(3):031901. https://doi.org/10.1063/1.3073717

67. Lan G, Liu S, Ma Y, Zhang X, Wang Y, Song Y. Sensitivity and figure-of-merit enhancements of liquid-prism SPR sensor in the angular interrogation. Optics Communications. 2015; 352:49–54. https://doi.org/10.1016/j.optcom.2015.04.046

68. Nair RR, Blake P, Grigorenko AN, Novoselov KS, Booth TJ, Stauber T, et al. Fine structure constant defines visual transparency of graphene. Science. 2008; 320(5881):1308–1308. https://doi.org/10.1126/science.1156965 PMID: 18388259

69. Liu PY, Chin L, Ser W, Chen H, Hsieh CM, Lee CH, et al. Cell refractive index for cell biology and disease diagnosis: past, present and future. Lab on a Chip. 2016; 16(4):634–644. https://doi.org/10.1039/C5LC01445J PMID: 26732872

70. Zhao H, Brown PH, Schuck P. On the distribution of protein refractive index increments. Biophysical Journal. 2011; 100(9):2309–2317. https://doi.org/10.1016/j.bpj.2011.03.004 PMID: 21539801

71. Ball V, Ramsden JJ. Buffer dependence of refractive index increments of protein solutions. Biopolymers: Original Research on Biomolecules. 1998; 46(7):489–492. https://doi.org/10.1002/(SICI)1097-0282(199812)46:7%3C489::AID-BIP6%3E3.0.CO;2-E

72. Huang Y, Yang C, Xu Xf, Xu W, Liu Sw. Structural and functional properties of SARS-CoV-2 spike protein: potential antivirus drug development for COVID-19. Acta Pharmacologica Sinica. 2020; 41(9):1141–1149. https://doi.org/10.1038/s41401-020-0485-4 PMID: 32747721

73. Lahiri B, McMeekin SG, Richard M, Johnson NP. Enhanced Fano resonance of organic material films deposited on arrays of asymmetric split-ring resonators (A-SRRs). Optics Express. 2013; 21(8):9343–9352. https://doi.org/10.1364/OE.21.009343 PMID: 23609645

74. Tong L, Wei H, Zhang S, Xu H. Recent advances in plasmonic sensors. Sensors. 2014; 14(5):7959–7973. https://doi.org/10.3390/s140507959 PMID: 24803189

75. Chao CTC, Chau YFC, Kooh MRR, Lim CM, Thotagamuge R, Chiang HP. Ultrawide bandstop filter with high sensitivity using semi-circular-like resonators. Materials Science in Semiconductor Processing. 2022; 151:106985. https://doi.org/10.1016/j.mssp.2022.106985

76. Fen YW, Yunus W, Yusof NA. Optical properties of cross-linked chitosan thin film for copper ion detection using surface plasmon resonance technique. Opt Appl. 2011; 41(4):999–1013.

77. Tombuloglu H, Sabit H, Al-Suhaimi E, Al Jindan R, Alkharsah KR. Development of multiplex real-time RT-PCR assay for the detection of SARS-CoV-2. Plos One. 2021; 16(4):e0250942. https://doi.org/10.1371/journal.pone.0250942 PMID: 33914804

78. Falzone L, Musso N, Gattuso G, Bongiorno D, Palermo CI, Scalia G, et al. Sensitivity assessment of droplet digital PCR for SARS-CoV-2 detection. International Journal of Molecular Medicine. 2020; 46(3):957–964. https://doi.org/10.3892/ijmm.2020.4673 PMID: 32705153

79. Alekseenko A, Barrett D, Pareja-Sanchez Y, Howard RJ, Strandback E, Ampah-Korsah H, et al. Direct detection of SARS-CoV-2 using non-commercial RT-LAMP reagents on heat-inactivated samples. Scientific Reports. 2021; 11(1):1–10. https://doi.org/10.1038/s41598-020-80352-8 PMID: 33469065

80. Funari R, Chu KY, Shen AQ. Detection of antibodies against SARS-CoV-2 spike protein by gold nanospikes in an opto-microfluidic chip. Biosensors and Bioelectronics. 2020; 169:112578. https://doi.org/10.1016/j.bios.2020.112578 PMID: 32911317

81. Rifat AA, Mahdiraji GA, Sua YM, Ahmed R, Shee Y, Adikan FM. Highly sensitive multi-core flat fiber surface plasmon resonance refractive index sensor. Optics Express. 2016; 24(3):2485–2495. https://doi.org/10.1364/OE.24.002485 PMID: 26906823

82. Haider F, Aoni RA, Ahmed R, Miroshnichenko AE. Highly amplitude-sensitive photonic-crystal-fiber-based plasmonic sensor. JOSA B. 2018; 35(11):2816–2821. https://doi.org/10.1364/JOSAB.35.002816

83. Li J, Han D, Zeng J, Deng J, Hu N, Yang J. Multi-channel surface plasmon resonance biosensor using prism-based wavelength interrogation. Optics Express. 2020; 28(9):14007–14017. https://doi.org/10.1364/OE.389226 PMID: 32403864

84. Kastritis PL, Bonvin AM. On the binding affinity of macromolecular interactions: daring to ask why proteins interact. Journal of The Royal Society Interface. 2013; 10(79):20120835. https://doi.org/10.1098/rsif.2012.0835 PMID: 23235262

85. Salahudeen MS, Nishtala PS. An overview of pharmacodynamic modelling, ligand-binding approach and its application in clinical practice. Saudi Pharmaceutical Journal. 2017; 25(2):165–175. https://doi.org/10.1016/j.jsps.2016.07.002 PMID: 28344466

86. René MH, Edward HC, Rachel BK, Kristin R, Sonia S, Shannon H, et al. Generation of high-affinity human antibodies by combining donor-derived and synthetic complementarity-determining-region diversity. Nature Biotechnology. 2005; 23(3):344–348. https://doi.org/10.1038/nbt1067

87. Mudgal N, Saharia A, Agarwal A, Ali J, Yupapin P, Singh G. Modeling of highly sensitive surface plasmon resonance (SPR) sensor for urine glucose detection. Optical and Quantum Electronics. 2020; 52:1–14. https://doi.org/10.1007/s11082-020-02427-0

88. Zheng W, Han B, Siyu E, Sun Y, Li X, Cai Y, et al. Highly-sensitive and reflective glucose sensor based on optical fiber surface plasmon resonance. Microchemical Journal. 2020; 157:105010. https://doi.org/10.1016/j.microc.2020.105010

89. Uddin SZ, Tanvir MR, Talukder MA. A proposal and a theoretical analysis of an enhanced surface plasmon coupled emission structure for single molecule detection. Journal of Applied Physics. 2016; 119 (20):204701. https://doi.org/10.1063/1.4952576

90. Konopsky VN, Alieva EV. Long-range propagation of plasmon polaritons in a thin metal film on a one-dimensional photonic crystal surface. Physical Review Letters. 2006; 97(25):253904. https://doi.org/10.1103/PhysRevLett.97.253904 PMID: 17280356

91. Ditlbacher H, Krenn JR, Schider G, Leitner A, Aussenegg FR. Two-dimensional optics with surface plasmon polaritons. Applied Physics Letters. 2002; 81(10):1762–1764. https://doi.org/10.1063/1.1506018

92. Hajati M, Hajati Y. Plasmonic characteristics of two vertically coupled graphene-coated nanowires integrated with substrate. Applied Optics. 2017; 56(4):870–875. https://doi.org/10.1364/AO.56.000870 PMID: 28158087

93. Moznuzzaman M, Islam MR, Hossain MB, Mehedi IM. Modeling of highly improved SPR sensor for formalin detection. Results in Physics. 2020; 16:102874. https://doi.org/10.1016/j.rinp.2019.102874

94. Kumar A, Yadav AK, Kushwaha AS, Srivastava S. A comparative study among WS_2, MoS_2 and graphene based surface plasmon resonance (SPR) sensor. Sensors and Actuators Reports. 2020; 2 (1):100015. https://doi.org/10.1016/j.snr.2020.100015

95. Akib TBA, Mou SF, Rahman M, Rana M, Islam M, Mehedi IM, et al. Design and Numerical Analysis of a Graphene-Coated SPR Biosensor for Rapid Detection of the Novel Coronavirus. Sensors. 2021; 21 (10):3491. https://doi.org/10.3390/s21103491 PMID: 34067769

96. Jia Y, Li Z, Wang H, Saeed M, Cai H. Sensitivity enhancement of a surface plasmon resonance sensor with platinum diselenide. Sensors. 2020; 20(1):131. https://doi.org/10.3390/s20010131

97. Bijalwan A, Singh BK, Rastogi V. Surface plasmon resonance-based sensors using nano-ribbons of graphene and WSe_2. Plasmonics. 2020; p. 1–9.